Annali Online dell'Università di Ferrara
Sezione Scienze della Terra
volume 2, fascicolo 1 (2014)

High resolution shallow geophysical methods for the investigation of the liquefaction phenomena: case study of the M_L 5.9 May 20th, 2012 Emilia earthquake (Italy)

Abu Zeid N.[1], Affatato A.[2], Baradello L.[2], Bignardi S.[1], Nieto Yàbar D.[2], Santarato G.[1]
[1] *Department of Physics and Earth Sciences, University of Ferrara, via Saragat 1, 44122 - Ferrara, Italy*
[2] *OGS- Istituto Nazionale di Oceanografia e di Geofisica Sperimentale, Borgo Grotta Gigante 42/C, 34010 - Sgonico (TS), Italy*
E-mail: *nsa@unife.it*
Received January 15, 2014

Abstract

A massive surface fracturing and sand ejection took place following the main shock of May 20th, 2012 earthquake (M_L=5.9 and hypocenter depth of 6.3 km), in the Emilia-Romagna Region, Northern Italy. These phenomena were induced by the liquefaction of a water-saturated, medium to coarse grained sand layer, laying at depths between 8 and 12 m below ground level. The occurrence of these co-seismic effects caused the damage of several buildings, many roads and sidewalks. In this work we describe the use of selected non-invasive high resolution geophysical methods to test their capability to characterize the subsurface of two sites were liquefaction events took place and possibly to map their extension at depth, especially those that reached the ground surface. The study is based on methods mapping the electric and electromagnetic properties of the subsurface materials, like Electrical Resistivity and Induced Polarization Tomography (ERT-IPT) and Ground Penetrating Radar (GPR). We present two case studies located at Mirabello village (ca 15 km to the SW of Ferrara), where both methods were applied. In test site No. 1, a two-dimensional (2D) ERT-IPT and one GPR profile were carried out, while in test site No. 2 a 3D ERT-IPT survey together with two GPR profiles were carried out. The obtained 2D/3D inversion models provided suggestive details about the surface ruptures extension at depth and in some sections succeeded in detecting the liquefied sand layer. The details are more evident on the IPT images rather than on the ERT ones, although clues about lateral spreading and densification of superficial sediments could be also deduced from the 2D ERT models. Similar results were also observed in the low frequency (70-100 MHz) GPR sections; however, the general applicability of this method is questionable because of the limited penetration depth due to the presence of fine grained soils and of a shallow water table depth. Based on the obtained results, which we consider as preliminary, the combined use of both ERT and IPT techniques can help achieving better lithostratigraphic models that can guide technicians in the proper selection of sites to be directly investigated by boreholes.

Keywords: liquefaction, surface ruptures, Induced Polarization, Electrical Resistivity Tomography, Ground Penetrating Radar

1. Introduction

Massive surface fracturing and sand ejection took place immediately after the main shock of May 20th, 2012 earthquake (M_L=5.9, depth: 6.3 km, min/max hypocentral distance to the test sites: 15-20 km), that stroke the Emilia-Romagna Region, Northern Italy. These phenomena, induced by the liquefaction of a shallow, water-saturated medium-to-coarse grained, sand layer, have resulted in the damage of several buildings as well as of roads and sidewalks. In particular, the liquefied sands were clustered along a narrow zone located between Sant'Agostino and Vigarano Mainarda villages (situated in the southwestern portion of Ferrara

Province), in correspondence to the palaeo-ridge of the Reno River (Papathanassiou *et al.*, 2012).

The Italian Building Code requires that Municipalities pertaining to seismic risk prone areas must develop first-order maps also describing zones prone to liquefaction. Previous and recent studies have already analyzed small, although sporadic, portions of the territories that may undergo liquefaction. The tools used for liquefaction risk evaluation are represented by the following geotechnical methods: CPT (Cone Penetration Test) and (more recently) CPTu (undrained CPT) and SCPTu (*i.e.* CPTu with shear wave measurement). However, the results of these methods, although providing a wealth of information about the subsurface, cannot be extended laterally with the same level of accuracy as at vertical of the test point. This urges the need for complementary investigation tools that can help in spatially extending the punctual information. Such improvements may come from the employment of shallow high resolution geophysical methods that are sensitive to texture, porosity and water content variations. The main purpose of their use is to enhance the spatial and vertical visibility of subsurface lithologic variations. This may allow for a better zoning of territories prone to liquefaction risk.

Due to the specific nature of the phenomenon, which involves the presence and movement of water and sand at shallow depths, the most suited methods for its geophysical imaging are those based on the electrical properties, mainly resistivity and dielectric permittivity.

Electrical Resistivity Tomography (ERT) is a well-known geophysical method that has already been successfully applied for active faults mapping, especially in palaeoseismological investigations (Caputo *et al.*, 2003; 2007). Likewise, the use of Ground Penetrating Radar (GPR) imaging is also well documented (*e.g.*, Gross *et al.*, 2002; Improta *et al.*, 2010; Ercoli *et al.*, 2013). Today, both methods can be considered consolidated tools for subsurface imaging in palaeoseismological investigations (McCalpin, 2009); however, their employment in the subsurface investigation of potentially liquefiable sites have received less attention (*e.g.* al-Shukri *et al.*, 2006; Liu and Li, 2001; Maurya *et al.*, 2006).

As to our knowledge, the use of the Induced Polarization (IP) method in liquefaction related studies is poorly documented in the literatures if not completely absent. Interested readers on the theoretical issues of the ERT and GPR methods can consult, among others, the text book of Reynolds (2011).

As concerns the IP method, a short description of its concept is provided in the following. The IP method is based on measuring the level of polarizability of subsurface materials. Polarizability is a physical phenomenon that can be explained by three mechanisms: i) electrode polarization, linked to the presence of mineral grains in water filled pores; ii) membrane polarization, linked to the presence of clay disseminated within a coarser grained sediments saturated with fresh water and iii) polarization due to constrictivity of fresh water filled pores, *i.e.* to the variation of their diameters (Schoen, 1996, Zadorozhnaya, 2008). Consequently, the IP is an electrical phenomenon which is independent on the above cited electrical properties. It can be measured either in time or in frequency domain. In the former way (Fig. 1a), the polarizability, defined as chargeability (*M*), represents the time integration of the decaying voltage at discrete time-windows, following current switch-off

$$M = \frac{1}{V_0}\int_{t_1}^{t_2} V_t dt \qquad [1]$$

where, M is the chargeability (ms), V_t voltage decay curve (mVolt), V_0 the initial voltage (Volt), while t_1-t_2 is the time window. In the latter way (Fig. 1b), polarizability is defined as a "Phase Shift", measured (in mrad) at a pre-defined frequency or as a "Percent Frequency Effect-PFE" (in %) where resistivity is measured at two different current injection frequencies. The "Phase" is simply obtained by taking the arctangent of the ratio of the imaginary to real components of the complex resistivity as expressed in Reynolds (2011).

Liquefaction is a process by which water-saturated sand and/or silty sand sediments temporarily loose their

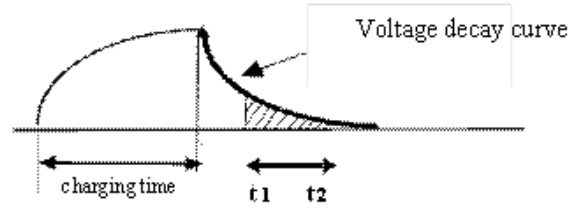

a)

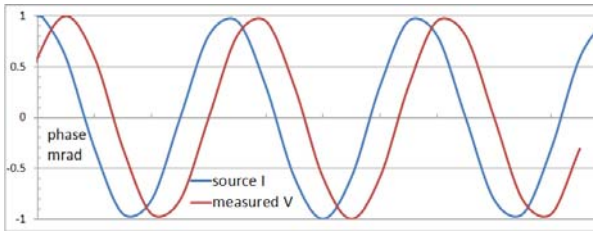

b)

Figure 1: Measured parameters of induced polarization a) in the time domain and b) in the frequency domain with the phase shift expressed in mrad (1 rad=1*180°/π=57.296°).

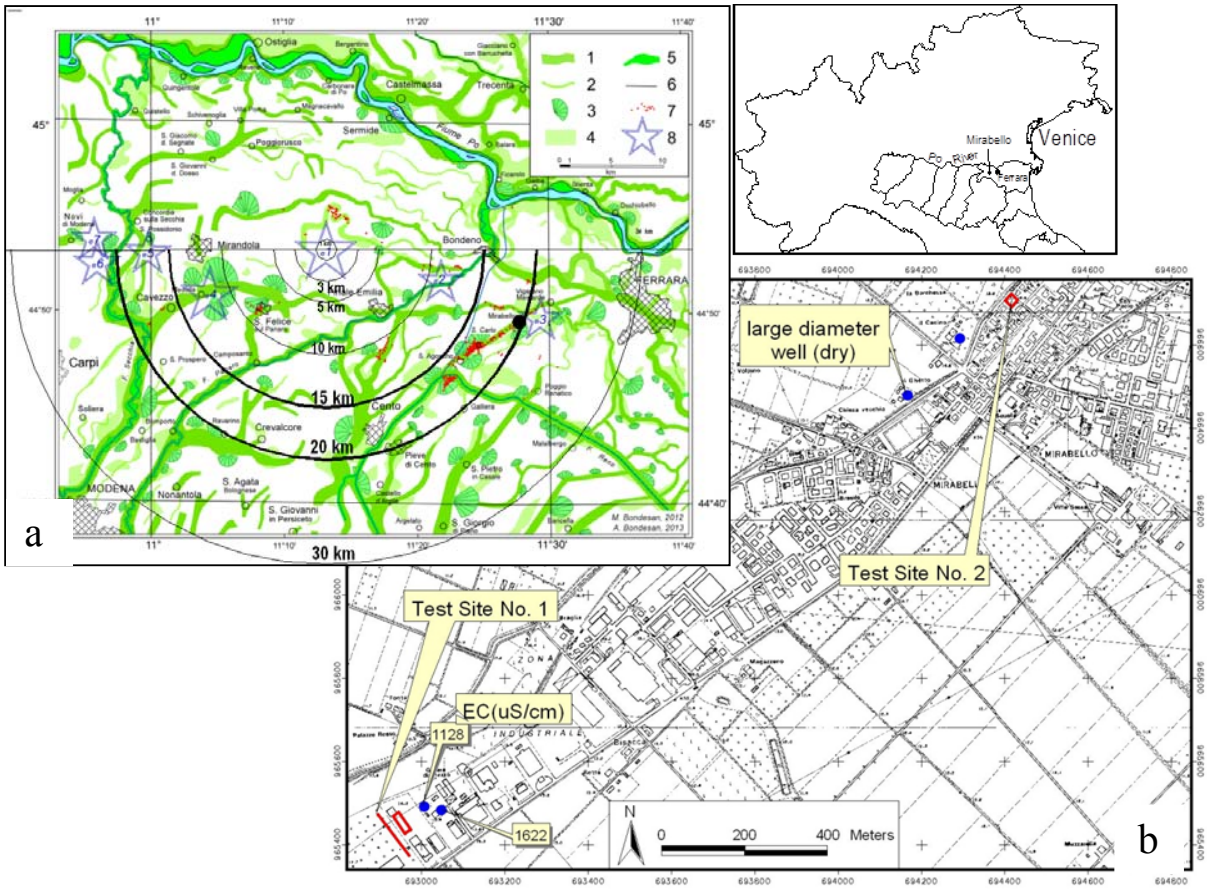

Figure 2: a) Simplified geomorphological map of the epicentral area showing the traces of the palaeo-rivers. Legend: 1) palaeo-river ridge; 2) palaeo-river; 3) sandy fluvial forms (palaeo-channels, fans); 4) other areas with prevalent sand deposits; 5) active flood plains; 6) river banks; 7) observed liquefaction point; 8) epi-centers of the M_L > 5.0 events occurred between May 20 and June 3, 2012 (e1: M_L=5.9, May 20th, 2012; e4: M_L=5.8, May 29th, 2012). The semi-circles indicate the distance from the epicenter of the May 20th, 2012 main shock. b) Topographic map showing the location of the investigated test sites (Nos. 1 and 2).

strength and act as a fluid, due to ground shaking when moderate to large earthquakes occur. This process results in high water pressure being exerted on the soil particles due to earthquake shaking. This may cause permanent deformations such as: formation of fractures and possible formation of sand boils, lateral spreading on gently dipping landforms and landslides in highly sloping terrains.

The IP technique is therefore a potentially useful tool to characterize both sand layers and mixed water/sand rising pathways. It is easily acquired by modern multi-electrode georesistivitymeters while resistivity measurements are being collected, so that a tomographic image of the subsurface is acquired with IP too (IPT). Likewise, inversion of IP data is generally an option of most available commercial program codes, which perform 2D/3D ERT data inversion, at the cost of a minor increment of the required time for processing. When we decided to test the IP method for the investigation of the liquefaction issue, we were well aware that using more independent methods will reduce possible ambiguities in geological interpretation.

ERT, IPT and GPR surveys were carried out together in two selected areas, located at Mirabello village (Ferrara Province, Northern Italy) where liquefaction has heavily damaged part of an industrial warehouse as well as other residential and religious buildings (Fig. 2).

The geophysical surveys, here described, aimed at imaging depth extension of the surface ruptures and possibly to reconstruct the geometry of the liquefied sandy layer(s). Geophysical data acquisition took place two to three weeks after the main shock when several geophysical teams were involved in a large-scale subsurface characterization campaign (*e.g.*, Abu Zeid *et al.*, 2012, Baradello *et al.*, 2012, Bellanova *et al.* 2012).

2. Geological and palaeogeographic outline

The Reno River outflows from the highly erodible Northern Apennines and it is therefore very rich in sedimentary load. The Reno alluvial plain records major lateral gradients of subsidence caused by both differential compaction (Carminati *et al.*, 2003) and by the persistent activity of blind faults characterizing this sector of the buried Apennines accretionary wedge. These tectonic structures has resulted in localized uplift in correspondence with the growth of fault-propagation anticlines during co-seismic reactivations. At this regard, recent DInSAR results (Atzori *et al.*, 2012) straightforwardly document the creation of topographic elevations (up to 20-25 cm) and topographic gradients as a consequence of the May 2012 co-seismic deformation. Evidence of cumulative effects during geological times are provided by several hydrographic anomalies well documented in the broader Po Plain (Burrato *et al.*, 2003; Castiglioni *et al.*, 1999).

In general, the area has experienced a large mobility of the hydrographical framework, whose evolution can be reconstructed and dated in great detail, based on the correlation of the stratigraphic-sedimentological evidence with a large number of ancient historical information and accurate old drawings, often related to unsuccessful hydraulic works.

During late Medioeval time, the investigated channel was generated through important crevasse episodes. From that time to the late XVIII century, the Reno water was able neither to reach directly the Adriatic Sea nor to directly inflow the Po River, running about 10 km to the north of the study area, therefore generating wide inland marshes and lakes. These fresh water areas were mainly developed in fast subsiding areas, between Ferrara and Bologna.

The depositional evolution of the area was punctuated by a large number of ill fated artificial embankments and land reclamation efforts. But it was only towards the end of the XVIII century that the Reno River was successfully forced to reach the sea through a former southern distributary channel of the Po River (Cremonini, 1988; Bondesan, 1989). The Reno water was diverted just to the south of the investigated site and any water flow northwards of Sant'Agostino was therefore impeded. The former channel dried up completely, thus well preserving its depositional morphology, only locally obliterated by modern anthropogenic activities. The elevated areas, corresponding to the levee sediments, were characterized by the availability of phreatic waters and by the comparatively good geotechnical properties for building. Accordingly, several settlements were located along the former channel body (*e.g.* levees), while the Modena-Ferrara road was running along the same path. The former levee crests are still commonly 5 m higher than the surrounding alluvial plain. Large topographic gradients still characterize the former channel area (Fig. 2a), inducing lateral variability of the overburden, which played a major role in the co-seismic liquefaction dynamics.

3. Data acquisition and analysis

3.1. Test site No. 1

In site 1 (industrial warehouse; Fig. 2b), high resolution ERT and IPT data were acquired along a 126 m-long profile, using 1 m electrode spacing, oriented in NW-SE direction *i.e.* perpendicular to the palaeo-ridge of the old Reno River. The ABEM SAS4000/ES464 georesistivitymeter (Sweden, *http://www.abem.se/products*) was employed for data acquisition. This equipment acquires IP information in the "time-domain" mode, *i.e.* by measuring the apparent chargeability (Fig. 1). As concerns the GPR survey, the data were collected using the DAD unit by IDS (Pisa, Italy.https://www.idscorporation.com/georadar/our-solutions-products) attached to a 70 MHz monostatic antenna by Radarteam (Sweden).

The ERT and IPT data were inverted using the RES2DINV (2012) commercial software that implements an inversion algorithm based on the smoothness-constrained least-squares method and uses the quasi-Newton approximation for optimization (Loke and Barker, 1996a). The inversion strategy is essentially of the Occam's type (deGroot-Hedlin and Constable, 1990; Sasaki, 1992).

The ERT and IPT 2D images are shown in figure 3. Field data were of good quality, as the RMS relative errors describing the discrepancy between field and predicted apparent resistivity data was 1.7% (percent RMS) and 0.75 (absolute RMS) for resistivity and chargeability models respectively.

The resistivity model (Fig. 3a) has identified two resistivity levels denoted a1 and a2. The former is characterized by resistivity values greater than 25 Ω.m, while the latter shows low resistivity values intercalated by local lateral heterogeneities. These low resistivity values can be associated with the presence of clay and silt sediments. The lateral heterogeneities, indicated by the letter A, show resistivity values between 20 and 40 Ω·m that can be attributed to the presence of silt and fine sand sediments, as probable local thickening of an otherwise continuous layer. This interpretation agrees with the direct subsurface information obtained from

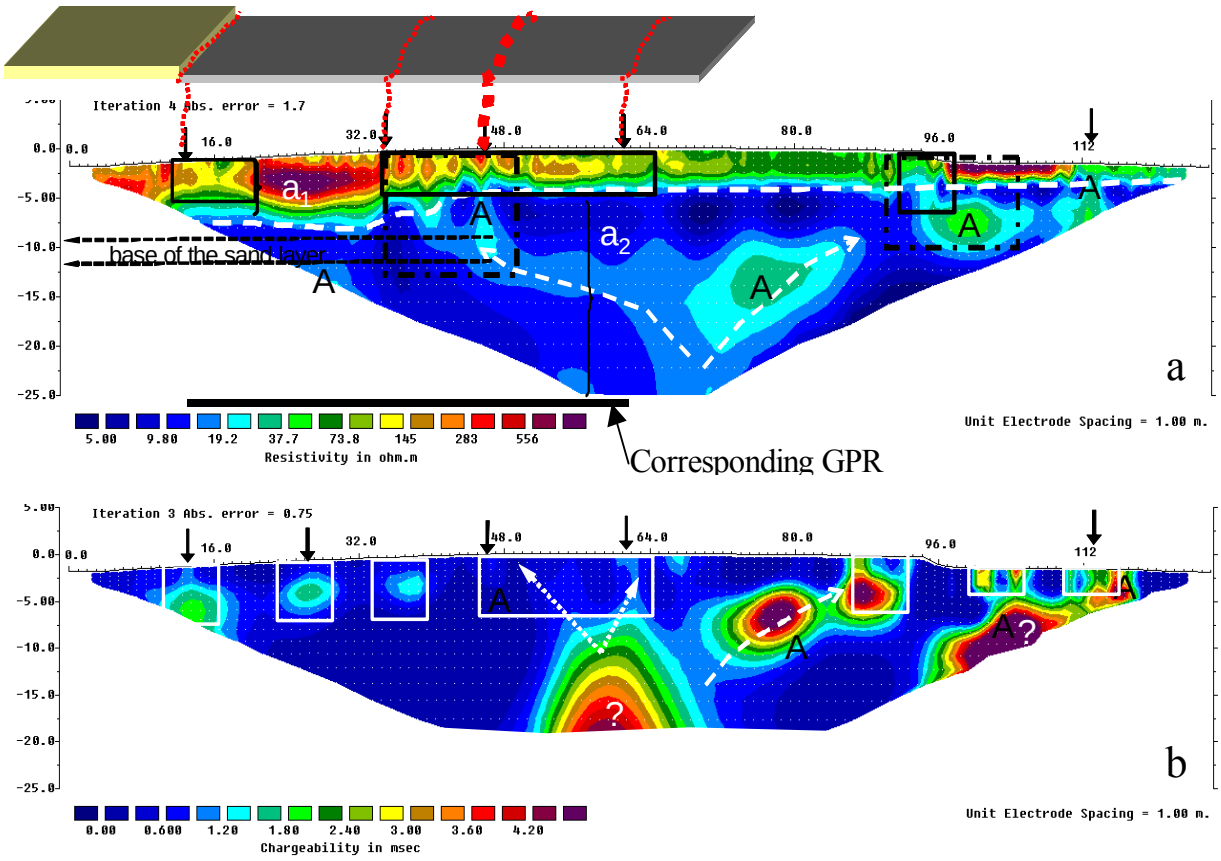

Figure 3: 2D inverted resistivity (a) and chargeability (b) models. a1 and a2 represent resistive and conductive horizons, respectively, while A is the resistivity anomaly due to lithological variation (silt and fine sand). Dashed white line is the possible palaeo-soil surface representing the top of the old embankment of the Reno River. The two shaded areas indicate the extension of the industrial building with respect to the profile. The left one represents the westernmost part of the warehouse severely damaged and subsequently demolished.

nearby boreholes. In these boreholes, a sandy silt layer was indeed encountered between 8.0 and 11.0 m-depth (Abu Zeid *et al.*, 2012).

Further analyses of the inversion models show that the first one presents lateral resistivity heterogeneities at 12 m, 35-65 m and around 96 m along the profile. These are likely associated with subsurface fractures whose traces were visible at the surface. One of these main fractures (at 35 m; Fig. 3a) has caused major damage to the industrial building located some 25 m towards north. Moreover, the resistivity anomaly, located at distance 48 m, was associated with the ejection of a modest amount of fine sand. This fact may be explained by the absence of the 3 m-thick layer of fine-grained sediments, which in contrast occurs in other areas (distances 35 to 95 m). It is interesting to note that the liquefied sand has moved horizontally towards NW and SE as suggested by the resistivity and chargeability models. Towards these directions, high density of surface ruptures is observed (rectangles in figure 3). It is worthmentioning that the local ground topography dips slightly towards NW where also a thick layer of saturated sand sediments is present. Moving towards SE, the models emphasize the presence of at least 2 m of low resistivity sediments (clay to clayey silt) below the surficial sediments located between 35 and 95 m. Their presence likely contributed in contrasting the local pore pressure increment.

The IPT model (Fig. 3b) evidences the occurrence of anomalies (indicated by rectangles) which are caused by variations in sediment texture (*i.e.* presence of silt and fine sand). The location of these anomalies is very near to the observed fractures indicating, in some cases, the probable pathway followed by the sand/water mixture. The most significant one is located between 45 and 64 m, where the trace of the nearly vertical fractures can be clearly inferred. Bearing in mind that polarizability of a

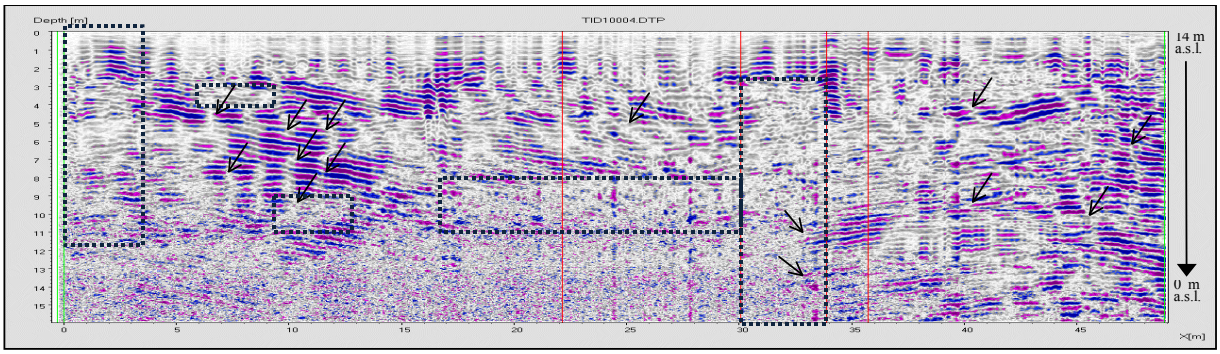

Figure 4: GPR section acquired parallel to a portion of the the ERT/IP (between 14 and 64 m). The profile is spatially shifted to the north (20 m) and vertically (-1.8 m) with respect to the ERT/IP profile position. Dashed rectangles: possible liquefied sand layers/levels, horizontal rectangle: liquefied sand layer. Arrows indicate subsurface extension of the fissure/dykes that in some cases have reached ground surface venting a mixture of sand and water (vertical rectangle shown in Fig. 4 between 30 and 35 m).

sediment is due to both presence of some percent of clay in pores and to pore-diameter variations, features, indicating possible upward migration of sediments can also been seen on the section between 75 and 90 m at ca. 7 m-depth.

Finally, the trace of the probable pathway followed by the sand/water mixture following the liquefaction of the sand layer, located at 8 to 12 m b.g.l., is evident at 45-80 m. The IPT shows the presence of localized anomalies which may be associated with probable zones that underwent liquefaction.

In the same area a 50 m-long GPR profile was carried out parallel to a portion of the ERT profile and located about 20 m northwards (Figs. 2b and 3). The collected data underwent simple processing steps including: trace normalization, time shift removal, dewowing, vertical BP filter, linear and logarithmic gain. An horizontal band pass filter was also applied, to remove horizontal bands with wave length greater than the profile length itself. We applied a velocity of 7 cm/ns, estimated by fitting a diffraction hyperbola, to calculate the depth of the reflecting horizons. The migrated GPR section (Fig. 4) shows clear reflections on both extremities of the profile slightly dipping in opposite directions. The lateral continuity of these reflections, although less evident in the central part, can be traced as well. For instance, reflections on the left side of the GPR section show the geometry of the palaeochannel sand deposits that agrees well with the ERT model. The reflections become less evident, if not absent, at depths greater than 10 m, which may indicate the top of the liquefied sand layer (between 0 and 15 m), as can be deduced by the high level of signal attenuation. The radargram suggests the presence of marked discontinuities indicated by arrows in figure 4, identified either by phase inversion or by abrupt horizontal disruptions. The traces of the ruptures terminate at some depth where reflection details are hardly visible. This is the case of the area evidenced by a horizontal rectangle (15 to 30 m) where probably the sand sediments underwent liquefaction. The depth of this layer is compatible with the resistivity and IP anomalies encountered at the same depth range.

Despite that little processing was necessary to enhance the radargram quality, we must keep in our minds that, in this specific case, low resistivity superficial sediments were absent, hence GPR signal attenuation was not so marked and did not limit the penetration depth as occurred in other sites where low resistivity superficial sediments highly attenuated the EM signal, hence reducing the penetration depth to 2 to 3 meters maximum. In fact, as shown in the Appendix, the EM theory shows that the penetration depth at an EM wave depends on the following physical parameters, *i.e.* electrical conductivity, dielectric permittivity and magnetic permeability, and on angular frequency of the signal (ω). Mathematically, these parameters constitute the so-called attenuation coefficient, α, as expressed in eq. [A5] (see Appendix).

3.2. Test site No. 2

In site No. 2, high resolution ERT, IPT and GPR surveys were carried out around a residential building at Mirabello village (Fig. 2b). The ERT and IPT data were collected using the LGM 4 Punkt light hp (Lippmann Geophysikalische Messgeräte, Germany: (*http://www.geophysik-dr-rauen.de/E_Index/E_GeoT*) georesistivitymeter. This equipment utilizes low frequency AC current to energize the subsurface; data

were collected using 4.16 Hz frequency. The IP effect was measured in the frequency domain by measuring the Phase Shift between the sinusoidal waveform of the injected current and that of the potential drop (Fig. 1b). In this case, the electrodes, spaced 1 meter apart, were installed around the perimeter of the building, *i.e.* forming a C-shaped electrode geometry (Figs. 2a and 5). Data were then collected all around the building, so as to allow for the investigation of the volumes beneath the building. This is an effective way to exclude the need to install electrodes inside the building itself (Santarato *et al.*, 2011). The pole-dipole array was used to collect the data, paying attention to get both forward and reverse measurements bearing in mind that it is an asymmetric array. A total of 1482 resistivity and phase shift readings were acquired.

Apparent resistivity and phase shift data were inverted using the commercial package ERTLab™ (developed jointly by Geostudi Astier, Italy and MPT, USA, http://www.geoastier.com/; www.mpt3d.com). The software generates a 3D mesh to account for the electrode geometry. The inversion process is performed following, once again, the Gauss-Newton method in a style similar to the Occam's inversion strategy. In this way, the best unbiased smooth resistivity and phase shift model parameters are obtained. The inversion algorithm verifies the fit of the model parameters by calculating the chi-squared error between simulated and experimental data. The best model is obtained once the chi-squared error ideally results in a misfit equal to the number of experimental data points. A view of the inverted 3D ERT and IPT models is shown in figure 6.

As concerns the resistivity model, the volumes underneath the building show low resistivity values (< 20 Ω·m) indicating the presence of fine-grained sediments (silt and clay) that have resulted from the presence of venting mixture of fine silt and mud. Moderate resistivity values (shown in red in figure 6a) correspond to slightly deformed pavement. In summary, the resistivity image does not provide clear clues about the effects of liquefaction (*i.e.* surface ruptures) despite the presence of a visible fracture (photo in figure 6a). The traces of these ruptures, however, are more evident in the IP image (Fig. 6b). In fact, the phase shift model shows high polarizability values in correspondence to the rupture traces and low to very low values underneath the building. This behavior can be explained by the accumulation of non-polarizable fine-grained sediments beneath the building and the accumulation of medium to coarse-grained sand, most probably mixed with a fraction of clay, in the fissures.

Grain size analyses conducted on a large number of vented sand boil samples have evidenced that the fine

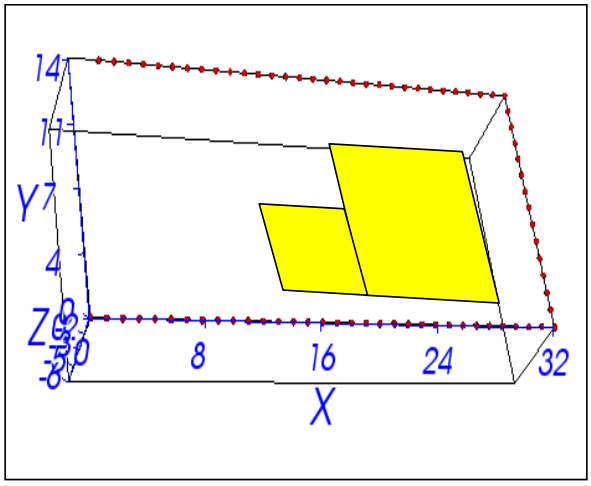

Figure 5: Layout of the electrodes (C-shaped rectangle of 32 m x 14 m) used to investigate the subsurface of the built area indicated by yellow colored parallelograms. Local altitude is 16.2 m.

percent was found to range between 10% and 30% with a number of samples that reached 45% (liquefied samples were collected on the ground surface and analyzed at the "Laboratorio Geotecnico Mucchi Antonio", Ferrara).

As concerns the GPR data, a GSSI SIR2000 equipment (*http://www.geophysical.com/aboutgssi.htm*, U.S.A.) attached to a 100 MHz monostatic antenna was utilized. We present in figure 7 two examples of GPR sections, although other antenna frequencies were tested (200 MHz and 400 MHz); the 100 MHz data show enough penetration depth and resolution and, most importantly ringing was absent. The processing flow used for data analysis followed three steps: gain, filtering and migration. After a spherical divergence correction the data were amplified using the Automatic Gain Control with 20 ns time window length. The plot of amplitude spectra was used to design the filter.

The spectra show a rapid attenuation at frequencies >80 MHz. Then the frequency band chosen for filtering were 30/40 – 100/130 MHz. To reproduce the subsurface features, we estimated a velocity of 8 cm/ns by fitting a diffraction hyperbola, while a Stolt-type migration was performed (also referred to as frequency-wavenumber migration; Stolt, 1978) and applied to migrate reflections to their true spatial position.

The processed sections show a series of wavy reflectors associated to clay-sand alternations. These layers locally exhibit ruptures and phase changing (red lines in figure 7) indicating the occurrence of liquefaction. The mixing sand-water probably was vented to the surface through these conducts or dykes.

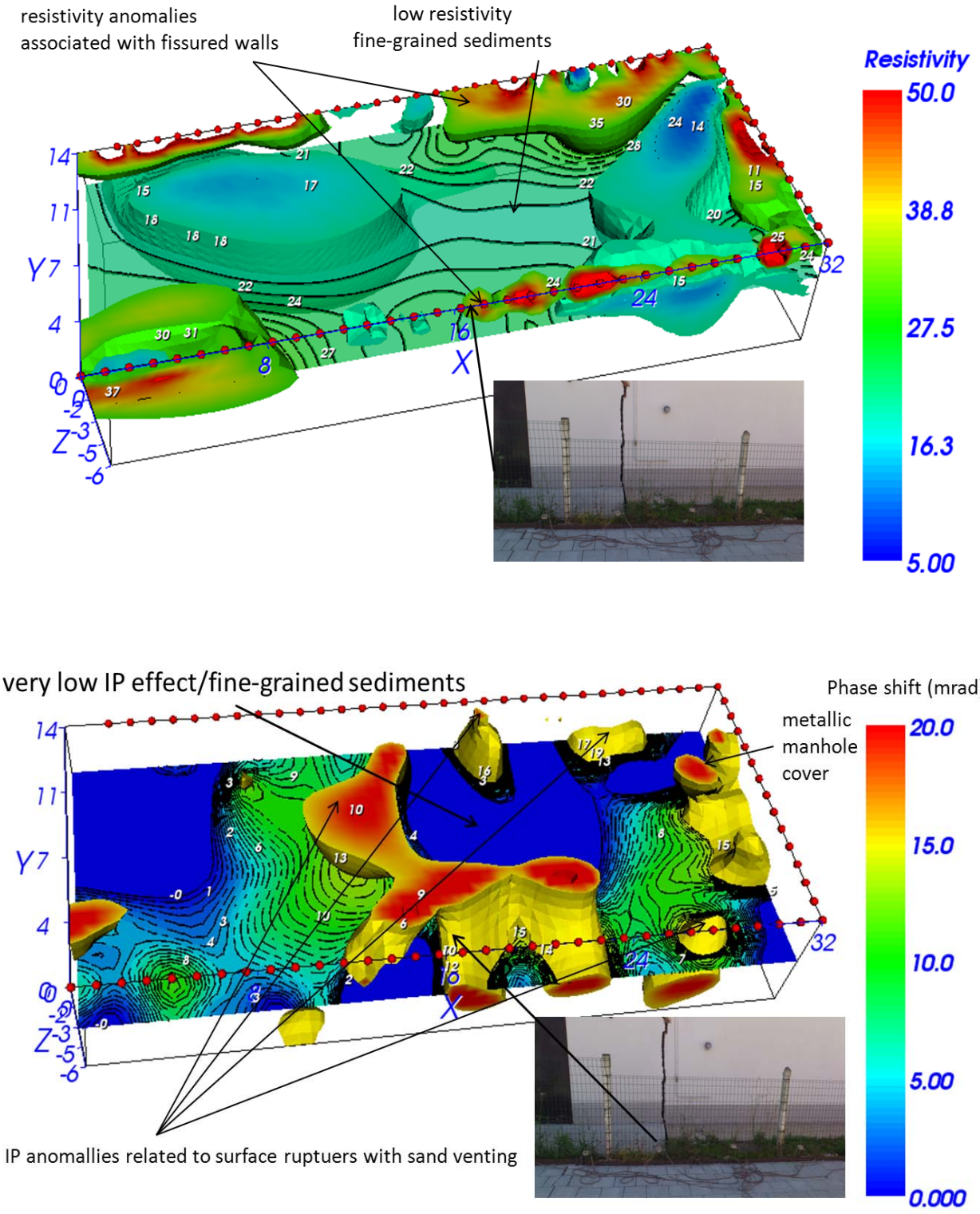

Figure 6: A view of the 3D inversion resistivity (a) and phase shift (b) models obtained for test site No. 2. The photograph shows a portion of the damaged external wall of the building due to liquefaction in the subsurface and consequent surface rupturing. Terrain elevation: 16.2 m a.s.l.

Discussion

The achieved results suggest that the combined use of electric and electromagnetic techniques can help in mapping the spatial and vertical distribution of co-seismic ruptures.

The contribution of the IP technique is relevant, as it was able to trace the most probable subsurface pathways or extension of the surface ruptures at depth. It also succeeded in highlighting those portions of the sand

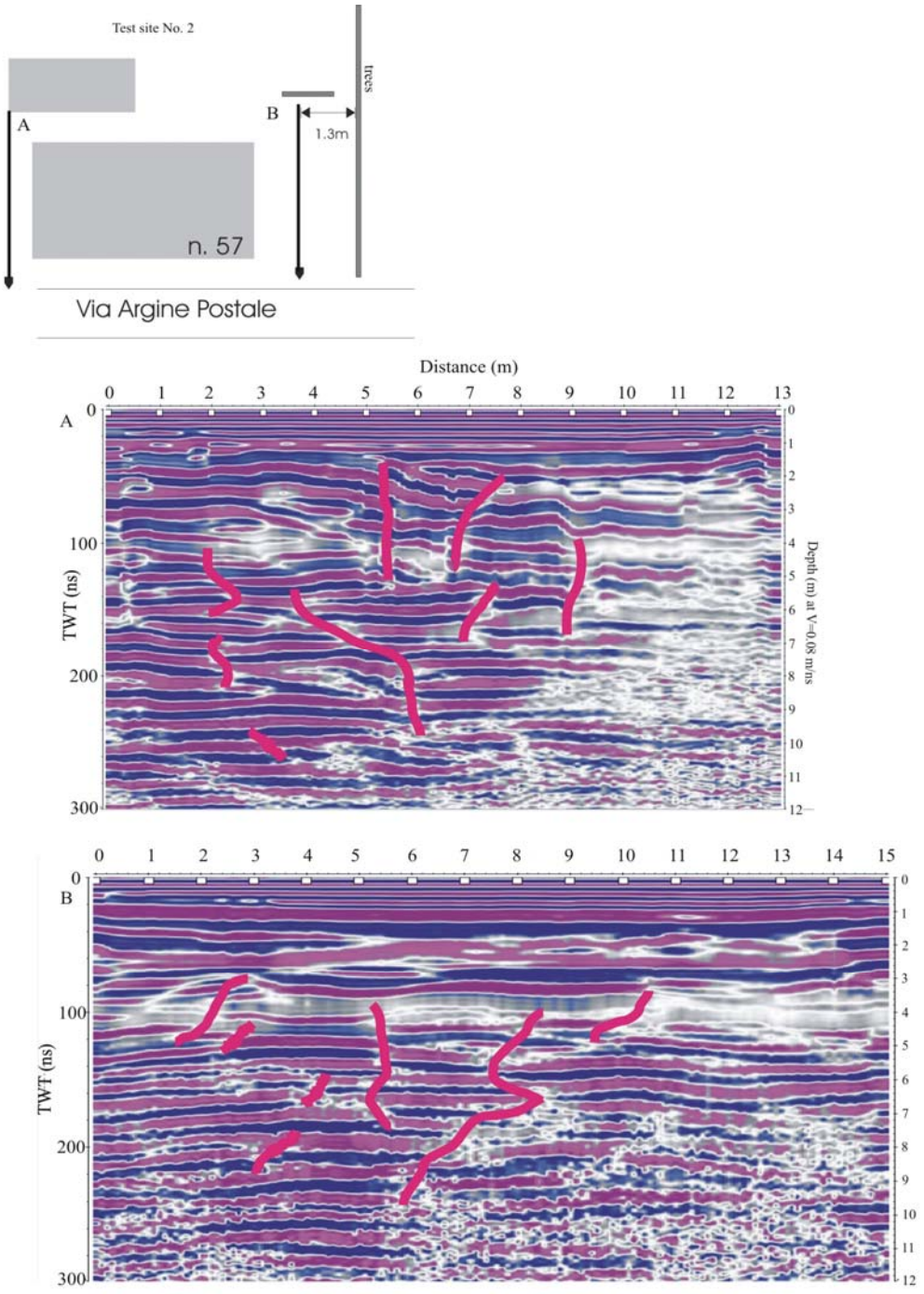

Figure 7: Two parallel GPR profiles collected at test site No. 2 (residential building). The inset map shows the location of the profiles. Thick red lines show the subsurface ruptures following liquefaction, which is evident beneath the right portion of the two radargrams (chainage > 9 m).

layers that underwent liquefaction. The observed agreement with the GPR sections suggests that, under favorable conditions, detailed analysis of the reflection attributes can identify the fractures and allow to trace their pathways to the maximum depth of penetration permitted by the specific ground conditions and the frequency of the used antenna.

The main outcome of this work concerns the benefit gained from the application of the IP method in the subsurface characterization of liquefied formations and in tracing the ruptures. This constitutes a useful tool for site characterization during the initial phases of reconstruction in areas already affected by such co-seismic effects. Finally, associated ERT and IPT may also be used to map and control consolidation effects normally used to mitigate the liquefaction risk. This last issue requires further tests and analyses in order to evaluate possibilities and limitations.

The non-invasiveness and repeatability of these methods, in addition to the capability of the IP technique to pinpoint lateral and vertical heterogeneities, represent the major points of force that can contribute both in mapping the geometry of sand layers that have already underwent liquefaction or in delimiting the subsurface spatial extension of sand layers that have high probability to undergo liquefaction.

Appendix

The EM theory shows that the penetration depth of the EM depends on four parameters: 1) relative permittivity (ε_r), 2) magnetic permeability (μ), 3) electrical conductivity (σ), and 4) the signal frequency (ω). The solution of Maxwell's equations for the propagation of a plain EM wave in the z direction (depth) is expressed mathematically as follows (Telford *et al.,* 1990):

$$E(z,t) = E_0 \cdot e^{i(\omega \cdot t - k \cdot z)} \qquad [A1]$$

where, E_0 represents the peak signal amplitude at surface and k the wavenumber (complex quantity) corresponding to

$$k = \alpha - i \cdot \beta, \;\; i = \sqrt{-1} \; . \qquad [A2]$$

α is the attenuation constant expressed in [Np/m] (it can be also expressed in decibel [db/m])

$$\alpha = \omega \cdot \left[\frac{\varepsilon_r \cdot \mu}{2} \left(\sqrt{1 + \tan^2 \delta} - 1 \right) \right]^2 \qquad [A3]$$

and β is the phase constant expressed in [rad/m]

$$\beta = \omega \cdot \left[\frac{\varepsilon_r \cdot \mu}{2} \left(\sqrt{1 + \tan^2 \delta} + 1 \right) \right]^2 \qquad [A4]$$

with

$$\tan^2 \delta \;\cong\; \frac{\sigma}{\omega \cdot \varepsilon_r} \qquad [A5]$$

where δ the skin depth, or else the depth at which the amplitude of the electric field decays to 1/e of its initial amplitude (or to ≈37% or ≈8.7 db) and $\tan^2(\delta)$ represents the loss tangent, or simply the energy loss due to faradic polarization (Knight and Endres, 2005). This approximation is valid only when the imaginary part of the relative permittivity and electrical conductivity are negligible.

The attenuation constant α (eq. [A4]) is also related to the skin depth (δ)

$$\alpha = \frac{1}{\delta} \qquad [A6]$$

5. References

Abu Zeid N., Bignardi S., Caputo R., Santarato G. and Stefani M. (2012): Electrical Resistivity Tomography investigations on liquefaction and fracturing phenomena at San Carlo, Italy. *Ann. Geophys.*, **55**(4), 713-716.

Al-Shukri H., Hanan M. and Tuttle M. (2006): Three-Dimensional Imaging of Earthquake-induced Features with Ground Penetrating Radar, Near Marianna, Arkansas. *Seismol. Res. Letts.*, **77**, 505-513.

Atzori S., Merryman Boncori J., Pezzo G., Tolomei C. and Salvi S. (2012): *Secondo Report analisi dati SAR e modellazione della sorgente del terremoto dell'Emilia.* INGV.

Baradello L., Accaino F., Affatato A., Nieto Yàbar D., Fanzutti F., Vaccaro C. and Abu-Zeid N. (2012): Indagini geofisiche speditive per l'analisi di strutture superficiali nell'area di Mirabello (FE). 31° Convegno Nazionale del Gruppo Nazionale di Geofisica della Terra Solida, Potenza 20-22/11/2012, *Atti*, 2, 5-9. ISBN 978-88-902101-2-9

Bellanova J., Dusi A., Gallipoli M.R., Giocoli A., Lizza C., Mucciarelli M., Piscitelli S., Stabile T.A. and Vignola L. (2012): L'intervento IMAA-CNR ed UNIBAS per il terremoto in Emilia: dati acquisiti e problematiche aperte. 31° Convegno Nazionale del GNGTS, Potenza 20-22/11/2012, *Atti*, 2, 10-13. ISBN 978-88-902101-2-9.

Bondesan M. (1989): Evoluzione geomorfologica e idrografica della pianura ferrarese. *Terre ed acqua*, Corbo Ed., 14-20

Burrato P., Ciucci F. and Valensise G. (2003): An inventory of river anomalies in the Po Plain, Northern Italy: evidence for active blind thrust faulting. *Ann. Geophys.*, **46**(5),

865-882.

Caputo R., Piscitelli S., Oliveto A., Rizzo E. and Lapenna V. (2003): The use of electrical resistivity tomography in Active Tectonic. Examples from the Tyrnavos Basin, Greece. *J. Geodyn.,* **36**, 19-35.

Caputo R., Salviulo L., Piscitelli S., Loperte A. (2007): Late Quaternary activity along the Scorciabuoi Fault (Southern Italy) as inferred from electrical resistivity tomographies. (Southern Italy) as inferred from electrical resistivity tomographies. Annals of Geophysics, **50**(2), 137-148.

Carminati E., Martinelli G. and Severi P. (2003): Influence of glacial cycles and tectonics on natural subsidence in the Po Plain (Northern Italy): Insights from 14C ages. *Geochemistry, Geophysics, Geosystems*, **4**(10), 1-14, doi:10.1029/2002GC000481.

Castiglioni G., Biancotti A., Bondesan M., Cortemiglia G.C., Elmi C., Favero V., Gasperi G., Marchetti G., Orombelli G., Pellegrini G.B. and Tellini C. (1999): Geomorphological map of the Po Plain, Italy, at a scale of 1:250.000. *Earth Surf. Proc. Landforms*, **24**, 1115-1120.

Constable S.C., Parker R.L. and Constable C.G. (1987): Occam's inversion, A practical algorithm for generating smooth models from electromagnetic sounding data. *Geophysics*, **52**, 289-300.

Cremonini S. (1988): Specificità dell'Alto Ferrarese nella problematica evolutiva dell'antica idrografia padana inferiore. In: *Bondeno ed il suo territorio dalle origini al Rinascimento*, Grafis Ed., Bologna, 17-24.

deGroot-Hedlin C. and Constable S. (1990): Occam's inversion to generate smooth, twodimensional models form magnetotelluric data. *Geophysics*, **55**, 1613-1624.

Ercoli M., Pauselli C., Frigeri A., Forte E. and Federico C. (2013): Geophysical paleoseismology" through high resolution GPR data: A case of shallow faulting imaging in Central Italy. *J. Appl. Geophys.*, **90**, 27-40.

Gross R., Green A.G., Horstmeyer H., Holliger K. and Baldwin J. (2003): 3-D georadar images of an active fault: efficient data acquisition, processing and interpretation strategies. *Subsurface Sensing Technologies and Applications*, **4**, 19–40.

Improta L., Ferranti L., De Martini P. M., Piscitelli S., Bruno P. P., Burrato P., Civico R., Giocoli A., Iorio M., D'Addezio G. and Maschio L. (2010): Detecting young, slow-slipping active faults by geologic and multidisciplinary high-resolution geophysical investigations: A case study from the Apennine seismic belt, Italy. *J. Geophys. Res.*, **115**, B11307, doi: 10.1029/2010jb000871.

Knight R. and Endres A.L. (2005): An introduction to rock physics for near surface applications. In: Butler *D.* (Ed.), *Near Surface Geophysics*, Concepts and Fundamentals, 1, 31-70, Soc. Expl. Geophys., Tulsa, Okla.

Lai C.G., Bozzoni F., Mangriotis M.-D. and Martinelli M. (2012): *Geotechnical aspects of May 20, 2012 M5.9 Emilia earthquake, Italy. European Centre for Training and Research in Earthquake Engineering*. http://www.geerassociation.org/GEER_Post%20EQ%20Reports/Italy_2012/2012_Emilia_Earthquake_Report.pdf.

Liu L. and Li Y. (2001): Identification of liquefaction and deformation features using ground penetrating radar in the New Madrid seismic zone, USA. *J. Appl. Geophys.*, **47**, 199-215.

Loke M.H. and Barker, R.D. (1996): Rapid least-squares inversion of apparent resistivity pseudosections by a quasi-Newton method. *Geophys. Prosp.*, **44**, 131-152.

Maurya D.M., Goyal B., Patidar A.K., Mulchandani N., Thakkar M.G. and Chamyal L.S. (2006): Ground Penetrating Radar imaging of two large sand blow craters related to the 2001 Bhuj earthquake, Kachchh, Western India. *J. Appl. Geophys.*, **60**, 142-152.

McCalpin J.P. (2009): *Paleoseismology*. Academic Press, Burlington, MA (USA), ISBN 978-0-12-373576-8.

Papathanassiou G., Caputo R. and Rapti-Caputo D. (2012): Liquefaction-induced ground effects triggered by the 20th May, 2012 Emilia-Romagna (Northern Italy) earthquake. *Ann. Geophys.*, **55**(4), 735-742, doi: 10.4401/ag-6147.

RES2DINV (2012). *Rapid 2-D Resistivity & IP inversion using the least-squares method*. http://www.geotomosoft.com/

Reynolds J.M. (2011): *An Introduction to Applied and Environmental Geophysics*, 2nd Edition. Wiley Blackwell, 712 pp., ISBN: 978-0-471-48536-0.

Santarato G., Ranieri G., Occhi M., Morelli G., Fischanger F. and Gualerzi D. (2011): Three-dimensional Electrical Resistivity Tomography to control the injection of expanding resins for the treatment and stabilization of foundation soils. *Eng. Geol.*, **119**, 18-30

Sasaki Y. (1992): Resolution of resistivity tomography inferred from numerical simulation. *Geophys. Prosp.*, **40**, 453-464.

Schoen J.H. (1996): *Physical Properties of Rocks: Fundamentals and Principles of Petrophysics*. Elsevier, 583 pp, ISBN-13: 978-0080410081.

Stolt R.H. (1978): Migration by Fourier Transform. *Geophysics*, **43** (1), 23-48.

Telford W.M., Geldart L.P. and Sheriff R.E. (1990): *Applied Geophysics*. Cambridge University Press, Cambridge (U.S.A.), pp. 770.

Zadorozhnaya V.Y. (2008): Resistivity measured by direct and alternating current: why are they different? *Advances in Geosciences*, **19**, 45-59.